Energies **2015**, *8*, 7441-7464; doi:10.3390/en8077441

OPEN ACCESS

energies

ISSN 1996-1073

www.mdpi.com/journal/energies

Article

Characteristic Analysis and Control of a Hybrid Excitation Linear Eddy Current Brake

Baoquan Kou *, Yinxi Jin, Lu Zhang and He Zhang

Department of Electrical Engineering, Harbin Institute of Technology, Harbin 150080, China;
E-Mails: jinyinxi2006@126.com (Y.J.); zhanglu24@hit.edu.cn (L.Z.); antonyamanda@163.com (H.Z.)

* Author to whom correspondence should be addressed; E-Mail: koubq@hit.edu.cn;
Tel./Fax: +86-451-8640-3771.

Academic Editor: Paul Stewart

Received: 31 March 2015 / Accepted: 17 July 2015 / Published: 22 July 2015

Abstract: In this paper, a novel hybrid excitation linear eddy current brake is presented as a braking system for high-speed road and rail vehicles. The presence of the permanent magnets (PMs), whose flux lines in the primary core are oppositely directed with respect to the flux lines by the excitation windings, has the effect of mitigating the saturation of the iron in the teeth of the primary core. This allows the brake to be fed with more intense currents, improving the braking force. First, using the magnetic equivalent circuit method and the layer theory approach, the analytical model of the hybrid excitation linear eddy current brake was developed, which can account for the saturation effects occurring in the iron parts. The saturation effects make the design and control of eddy current brakes more difficult. Second, the relationship between the braking force characteristics and the design parameters were analyzed to provide useful information to the designers of eddy current brakes. Then, the controller of the hybrid excitation linear eddy current brake was designed to control the amplitude of the braking force. Finally, experimental measurements were conducted to verify the validity of the theoretical analysis.

Keywords: eddy current brake; hybrid excitation; finite element method; three-level pulse-width modulation (PWM) scheme

---

1. Introduction

The use of and research on eddy current brakes in high-speed road and rail vehicles have gradually increased [1–9]. Relative to the traditional mechanical friction brake, the eddy current brake has the advantages of no mechanical contact, high reliability, long working life, and lower sensitivity to environmental parameters, such as temperature and aging. Eddy current brakes have excellent braking performance, especially at high speed.

In eddy current brakes, the magnetic field can be produced by excitation winding systems or by permanent magnets. According to differences of the flux sources, eddy current brakes can be divided into three types: electric excitation eddy current brakes, permanent magnet eddy current brakes and hybrid excitation eddy current brakes. For the electric excitation eddy current brakes, the braking force can be adjustable, but an additional power supply system is required, and the braking force density is low. The permanent magnet eddy current brakes allow for elimination of the electrical supply system to simplify the device structure, but conversely, braking force modulation is not allowed, and magnet corrosion and relatively low temperature tolerance are potential hazards. The hybrid excitation eddy current brakes are a combination of the permanent magnet eddy current brakes and the electric excitation eddy current brakes and exhibit the advantages of both. Therefore, the amplitude of the braking force density is large and adjustable, and the excitation loss is low. Moreover, according to differences in the structure, eddy current brakes can be classified as radial [10–12], axial [13,14], or linear [15–17].

Analysis of and research on eddy current brakes can be found in many papers. Gay *et al.* [18] analyzed the relationship between the braking force and the design parameters using the analytical method and the finite element method, respectively, and experimental validation was carried out. However, the experiment results did not agree with the calculated results well. Canova *et al.* [19] presented an analytical model of the eddy current brake considering a 3D analytical correction. Then, the validity of the 3D analytical model was verified using 3D finite element simulations. Yazdanpanah *et al.* [20] developed a subdomain-based analytical model and evaluated the performance characteristics and design considerations of the device by using the analytical model. The validity of the analytical model was verified through the 3D finite element method and experimental measurement. The experimental results of the prototype brake verified the investigations and the design. In addition to the above studies, many researchers have focused on the analytical model of eddy current brakes [21–25], and the saturation effects occurring in the iron parts were omitted in most of these calculation models. Moreover, thus far, the analytical model of hybrid excitation eddy current brakes has been little studied.

In this paper, a novel hybrid excitation linear eddy current brake is presented. The remainder of this paper is organized as follows: in Section 2, the structure and working principle of the hybrid excitation linear eddy current brake are explained. The analytical model of the hybrid excitation linear eddy current brake, which can account for the saturation effects occurring in the iron parts, is deduced in Section 3. In Section 4, the parameter analysis is provided, and the controller is designed in Section 5. A three-level PWM scheme is used to reduce the switching frequency and excitation current harmonics. In Section 6, the experimental verification is carried out, and the paper is concluded in Section 7.

2. Structure and Working Principle of the Hybrid Excitation Linear Eddy Current Brake

2.1. Structure of the Hybrid Excitation Linear Eddy Current Brake

The hybrid excitation linear eddy current brake includes the primary part and the secondary part, as shown in Figure 1. The primary part consists of the excitation windings, the primary core and the permanent magnets. The permanent magnets are polarized parallel to the direction of the movement of the mover, and they are placed in notches with alternate polarity. The secondary part comprises a low resistivity conductor plate (in this paper, copper is used) on an iron backing.

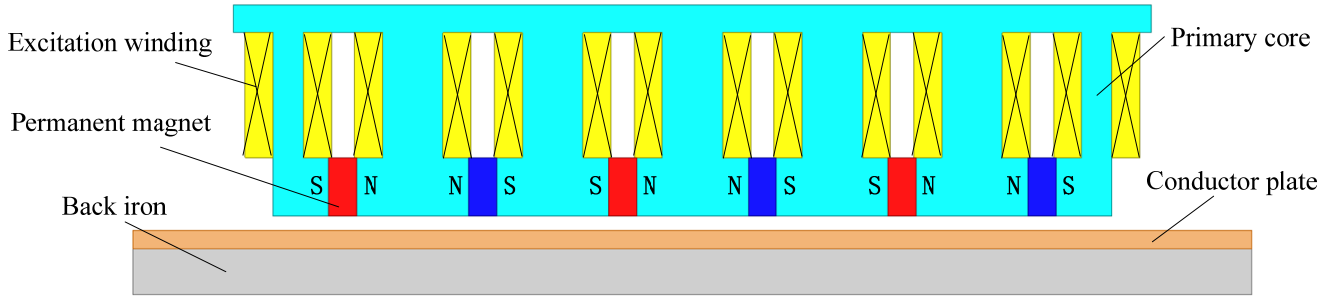

Figure 1. Structure of the hybrid excitation linear eddy current brake.

2.2. Working Principle of the Hybrid Excitation Linear Eddy Current Brake

When the excitation windings are without excitation current, the flux generated by the permanent magnets will form a magnetic short-circuit ring in the primary iron core, and it almost does not pass through the air gap, as shown in Figure 2a. When excitation current flows through the excitation windings, there are two flux loops, as shown in Figure 2b.

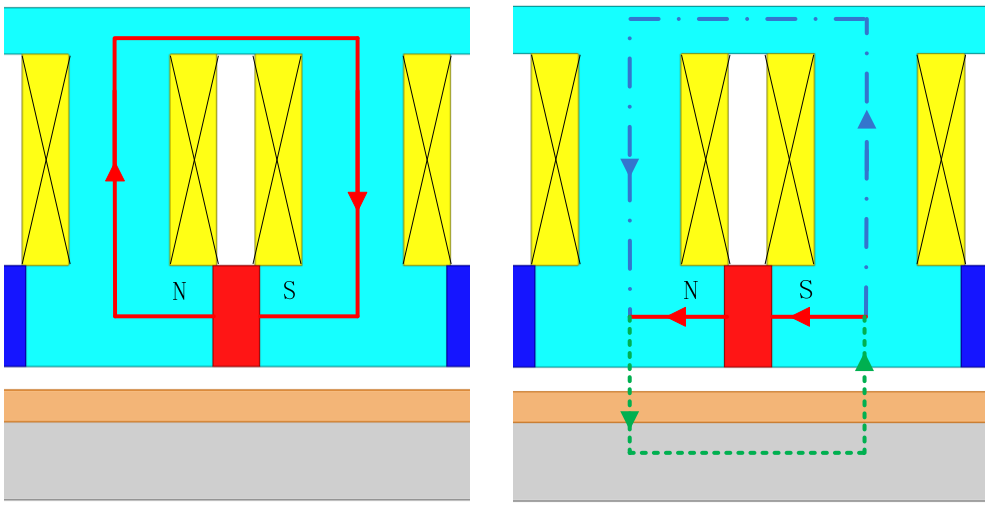

(**a**) (**b**)

Figure 2. Flux flow: (**a**) excitation windings without excitation current and (**b**) excitation windings with excitation current.

One is produced by the excitation windings, and the other is produced by the permanent magnets. The solid line is the flux produced by the permanent magnets, the dot and dash line is the flux produced by the excitation windings, and the dotted line is the total flux produced by the permanent magnets and the excitation windings. According to the law of electromagnetic induction, the relative movement of the primary part and the secondary conductor plate causes eddy currents in the conductor plate. Due to the interactions of the eddy currents and the magnetic flux generated by the permanent magnets and the excitation windings, the braking force between the primary part and the secondary part is produced.

3. Analytical Model

In this section, the analytical model of the hybrid excitation linear eddy current brake is derived. The purpose is to rapidly provide insight into the fundamental physics of the eddy current brake and preliminary design data that verify whether the performance and size are compatible with the envisioned application.

3.1. Static Field Analysis

In order to build the analytical model of the hybrid excitation linear eddy current brake, the static field is analyzed. The definition of iron part reluctances and the magnetic equivalent circuit are shown in Figure 3. All elements of the magnetic equivalent circuit are calculated in detail below. The ampere-turns of an excitation winding are as follows:

$$F_{\mathrm{f}} = NI \tag{1}$$

where N and I are the turns of the excitation windings and the excitation current, respectively. The MMF (magnetic motive force) of a permanent magnet is as follows:

$$F_{\mathrm{c}} = H_{\mathrm{c}} h_{\mathrm{m}} \tag{2}$$

where H_{c} and h_{m} are the coercivity and width of the permanent magnets, respectively. According to Figure 3a, the iron part reluctances are calculated as follows:

$$R_{\mathrm{l}} = \frac{\tau - h_{\mathrm{m}}}{2\mu_0\mu_{\mathrm{l}} l_\delta b_{\mathrm{m}}} \tag{3}$$

where τ is the pole pitch, μ_0 is the air permeability, μ_{l} is the relative permeability of R_1, l_δ is the width of the primary core, and b_{m} is the height of the permanent magnets.

$$R_2 = \frac{h_{\mathrm{s}} + \frac{b_{\mathrm{m}}}{2} + \frac{h_{\mathrm{j}}}{2}}{\mu_0\mu_2 l_\delta b_{\mathrm{t}}} \tag{4}$$

where h_{s} is the height of slot, h_{j} is the height of the primary yoke, μ_2 is the relative permeability of R_2, and b_{t} is the tooth width.

$$R_3 = \frac{\tau}{\mu_0\mu_3 l_\delta h_{\mathrm{j}}} \tag{5}$$

where μ_3 is the relative permeability of R_3.

$$R_4 = \frac{b_m}{2\mu_0\mu_4 l_\delta(\tau - h_m)} \tag{6}$$

where μ_4 is the relative permeability of R_4.

$$R_5 = \frac{h_b}{2\mu_0\mu_5 l_\delta(\tau - h_m)} \tag{7}$$

where h_b is the thickness of the back iron, and μ_5 is the relative permeability of R_5.

$$R_6 = \frac{\tau}{\mu_0\mu_6 l_\delta h_b} \tag{8}$$

where μ_6 is the relative permeability of R_6. The reluctances of the air gap and conductor plate are calculated as follows:

$$R_c = \frac{c}{\mu_0\mu_c l_\delta(\tau - h_m)} \tag{9}$$

where c is the conductor plate thickness, and μ_c is the relative permeability of the conductor plate.

$$R_\delta = \frac{\delta}{\mu_0 l_\delta(\tau - h_m)} \tag{10}$$

where δ is the air gap length. According to the magnetic equivalent circuit, the following equations are provided:

$$2F_f - F_{AB} = 2\phi_r R_2 + \frac{\phi_r}{2} R_3 \tag{11}$$

$$F_c - F_{AB} = R_m\phi_m + 2R_1\phi_m \tag{12}$$

$$F_{AB} = R_6\phi_\delta/2 + \phi_\delta(2R_4 + 2R_5 + 2R_\delta + 2R_c) \tag{13}$$

$$\phi_\delta = 2\phi_m + \phi_r \tag{14}$$

where F_{AB} is the MMF between points A and B, and ϕ_r, ϕ_m and ϕ_δ are the flux of the loops shown in Figure 3.

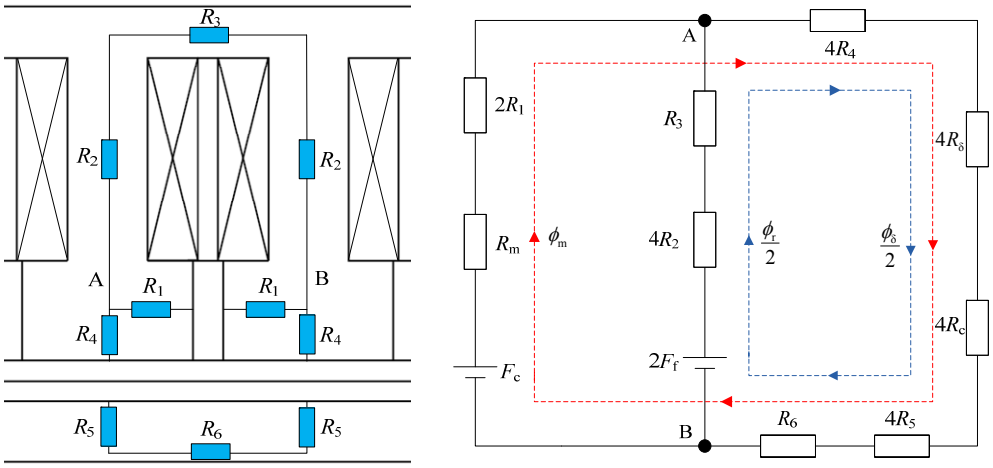

(**a**) (**b**)

Figure 3. (**a**) Definition of iron part reluctances and (**b**) the magnetic equivalent circuit.

Thus, it is possible to calculate the amplitude of the air gap flux density:

$$B_0 = \frac{\phi_\delta}{l_\delta(\tau - h_m)} \tag{15}$$

In many researches, the air gap flux density is assumed as a rectangular wave. But the actual air gap flux density waveform is not a rectangular wave, as shown in Figure 4. Therefore in this paper, the air gap flux density waveform for different design parameters is calculated based on the finite element method (FEM), and an empirical piecewise function is proposed to fitting the actual air gap flux density waveform.

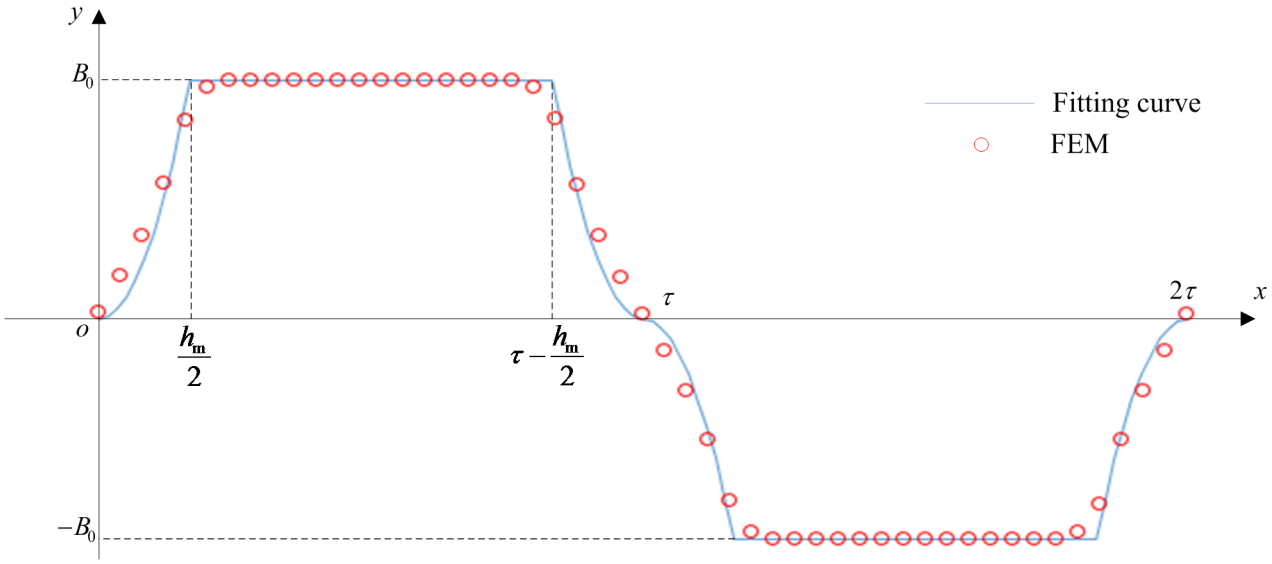

Figure 4. Waveform of the air gap flux density at the speed of 0 m/s.

The expression of the piecewise function is shown below:

$$f(x) = \begin{cases} \frac{4B_0}{h_m^2}x^2 & 0 \le x \le \frac{h_m}{2} \\ B_0 & \frac{h_m}{2} \le x \le \tau - \frac{h_m}{2} \\ \frac{4B_0}{h_m^2}(x-\tau)^2 & \tau - \frac{h_m}{2} \le x \le \tau \\ -\frac{4B_0}{h_m^2}(x-\tau)^2 & \tau \le x \le \tau + \frac{h_m}{2} \\ -B_0 & \tau + \frac{h_m}{2} \le x \le 2\tau - \frac{h_m}{2} \\ -\frac{4B_0}{h_m^2}(x-2\tau)^2 & 2\tau - \frac{h_m}{2} \le x \le 2\tau \end{cases} \tag{16}$$

Therefore, based on the Fourier decomposition, the air gap flux density is expressed as:

$$B_{\delta n} = \frac{4}{\tau}\int_0^{\frac{\tau}{2}} f(x)\cdot\sin\left(\frac{n\pi x}{\tau}\right)dx \quad n=(1,3,5\cdots) \tag{17}$$

$$B_{\delta} = \sum_{n}^{\infty} B_{\delta n} \mathrm{e}^{jkx} \tag{18}$$

$$k = \frac{n\pi}{\tau} \tag{19}$$

The specific procedure is explained in below: Firstly, the amplitude of the air gap flux density B_0 is calculated using the magnetic equivalent circuit. Then, the waveform of the air gap flux density is obtained based on the empirical piecewise function. Finally, the expression of the air gap flux density is deduced using the Fourier decomposition.

3.2. Braking Force Analysis

A complete 3-dimensional analytical solution for the hybrid excitation linear eddy current brake proposed in this paper is difficult and will not be attempted. Instead, the configuration of a 2-dimensional layer model, shown in Figure 5, will be used for the analysis.

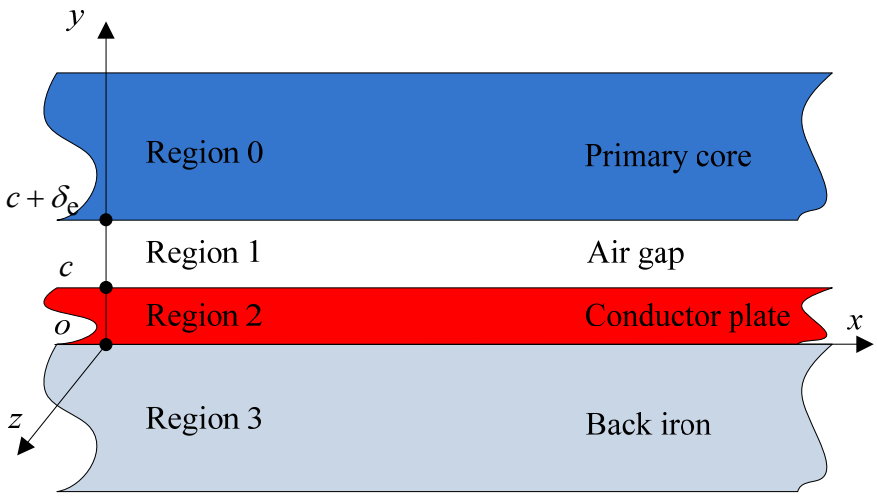

Figure 5. Two-dimensional multi-layer model.

The multi-layer model is divided into four different regions:

Region 0: primary core.
Region 1: air gap.
Region 2: secondary conductor plate.
Region 3: back iron.

In order to simplify the analysis, the following assumptions are made. The primary core, conductor plate and back iron are considered to be infinitely long in the *x*-direction. All currents are in the *z*-direction. The excitation winding, permanent magnets and salient poles are replaced by infinitely thin linear current sheets backed by smooth iron boundaries. These linear current sheets are chosen in such a way that they provide the same field in the air gap of the model having smooth structures that the original excitation windings and permanent magnets produced in the actual machine. In such a case, the actual air gap δ of the machine is replaced, using Carter's coefficient, by an effective air gap δ_e that accounts for the interpolar space and variable reluctance.

On the plane $y = c + \delta_e$, there are infinitely thin current sheets flowing in the z-direction. This current can be expressed as:

$$J_s(x) = \sum_n^{\infty} J_n \sin(kx + \pi) \tag{20}$$

$$\delta_e = K_\delta \delta \tag{21}$$

where J_n is the amplitude of the harmonics, and K_δ is Carter's coefficient.

The MMF that is produced by the infinitely thin linear current sheet is:

$$at = \sum_n^{\infty} \int_0^x J_n \sin(kx + \pi) dx = \sum_n^{\infty} \frac{J_n}{k} \cos(kx) \tag{22}$$

Based on the above assumptions, the air gap flux density produced by the infinitely thin linear current sheet is the same as that of Equation (18), therefore the following expression can be obtained:

$$\frac{\mu_0 \times at}{c + \delta_e} = \mathrm{Re}(B_\delta) \tag{23}$$

$$J_n = k(c + \delta_e) \frac{B_{\delta n}}{\mu_0} \tag{24}$$

The electromagnetic equation expressed in terms of the magnetic vector potential $\boldsymbol{A}$ is:

$$\nabla^2 \boldsymbol{A} = -\mu_j \mu_0 \boldsymbol{J} \tag{25}$$

This equation has to be written for each region.

Region 1: in the air gap, the conductivity is zero and the field equation is:

$$\nabla^2 \boldsymbol{A}_1 = 0 \tag{26}$$

In order to solve the second-order differential equation system, the variable separation method has been adopted, and, to simplify the problem, we can assume that all the electromagnetic quantities are periodic with pole pitch, which means:

$$\boldsymbol{A}(x, y) = \boldsymbol{A}(y) e^{jkx} \tag{27}$$

Therefore, the general solution is shown as:

$$A_{1n}(y) = C_{1n} e^{ky} + D_{1n} e^{-ky} \tag{28}$$

where C_{1n} and D_{1n} depend on the boundary conditions.

Region 2: this is the only one made of conductive material, and the field equation is:

$$\nabla^2 \boldsymbol{A}_2 = -\mu_c \mu_0 \boldsymbol{J}_2 \tag{29}$$

From Faraday laws:

$$\boldsymbol{J}_2 = -\sigma_c v \frac{\partial \boldsymbol{A}_2}{\partial x} \tag{30}$$

where σ_c is the conductivity of conductor plate and v is the speed.

Finally, the field equation becomes:

$$\boldsymbol{A}_2''(y) = \left(jk\mu_c\mu_0\sigma_c v + k^2\right)\boldsymbol{A}_2(y) \tag{31}$$

$$A_{2n}(y) = C_{2n}e^{\lambda y} + D_{2n}e^{-\lambda y} \tag{32}$$

where C_{2n} and D_{2n} depend on the boundary conditions and the exponential coefficient is:

$$\lambda = \sqrt[4]{k^4 + \left(k\mu_c\mu_0\sigma_c v\right)^2}\,e^{j\theta} \tag{33}$$

$$\theta = \frac{1}{2}\arctan\left(\frac{\mu_c\mu_0\sigma_c v}{k}\right) \tag{34}$$

Region 3: assuming that the conductivity in the back iron is zero, the field equation is:

$$\nabla^2\boldsymbol{A}_3 = 0 \tag{35}$$

$$A_{3n}(y) = C_{3n}e^{ky} + D_{3n}e^{-ky} \tag{36}$$

In the multi-layer model, we have considered that region 3 is extended from $y = 0$ to $y = -\infty$, thus:

$$\boldsymbol{A}_3(-\infty) = 0 \tag{37}$$

Therefore, the general solution is shown as:

$$A_{3n}(y) = C_{3n}e^{ky} \tag{38}$$

where C_{3n} depends on the boundary conditions.

The boundary conditions are shown as follows:

Between region 0 and region 1:

$$\frac{\partial A_{1n}(c+\delta_e)}{\partial y} = \mu_0 J_n \tag{39}$$

Between region 1 and region 2:

$$\left\{\begin{matrix} B_{1n} = B_{2n} \\ H_{1n} = H_{2n} \end{matrix}\right.\Bigg|_{y=c} \tag{40}$$

Between region 2 and region 3:

$$\left\{\begin{matrix} B_{2n} = B_{3n} \\ H_{2n} = H_{3n} \end{matrix}\right.\Bigg|_{y=0} \tag{41}$$

where μ_b is the relative permeability of the back iron and, in this paper, we assume that:

$$\mu_b = \mu_6 \tag{42}$$

It is possible to calculate the eddy current loss in the conductor plate:

$$P_e = \sum_n^{\infty} pl_\delta\sigma_c v^2 k^2 |S|^2 \tau\left(\frac{e^{2k_1 c}}{2k_1} - \frac{e^{-2k_1 c}}{2k_1} + \frac{2\sin(k_2 c)\cos(k_2 c)}{k_2}\right) \tag{43}$$

$$k_1 = \mathrm{Re}(\lambda) \tag{44}$$

$$k_2 = \mathrm{Im}(\lambda) \tag{45}$$

$$S = C_{2n} = D_{2n} \tag{46}$$

where p is the number of pole-pairs.

Finally, the braking force is calculated as:

$$F = \frac{P_e}{v} = \sum_n^{\infty} p l_\delta \sigma_c v k^2 |S|^2 \tau \left(\frac{e^{2k_1 c}}{2k_1} - \frac{e^{-2k_1 c}}{2k_1} + \frac{2\sin(k_2 c)\cos(k_2 c)}{k_2} \right) \tag{47}$$

3.3. Consideration of the Nonlinear Magnetization Characteristics of the Iron Core

The nonlinearity magnetization characteristics of the iron core material are a problem in the analysis of the eddy current brake because the typical operational condition of the eddy current brake requires a high supplied excitation current.

In order to address the nonlinearity of the iron core material, the iterative procedure is used. It starts by assigning an initial value to μ_1, μ_2, μ_3, μ_4, μ_5 and μ_6 to determine the reluctances of the iron core part and calculate the circuit fluxes. Next, the magnetic flux densities within R_1, R_2, R_3, R_4, R_5 and R_6 are calculated. Then, based on the *B-H* curve of the utilized steel, new relative permeabilities μ'_1, μ'_2, μ'_3, μ'_4, μ'_5 and μ'_6 can be obtained. The process continues until the criterion is individually satisfied for all relative permeabilities, as shown in Figure 6.

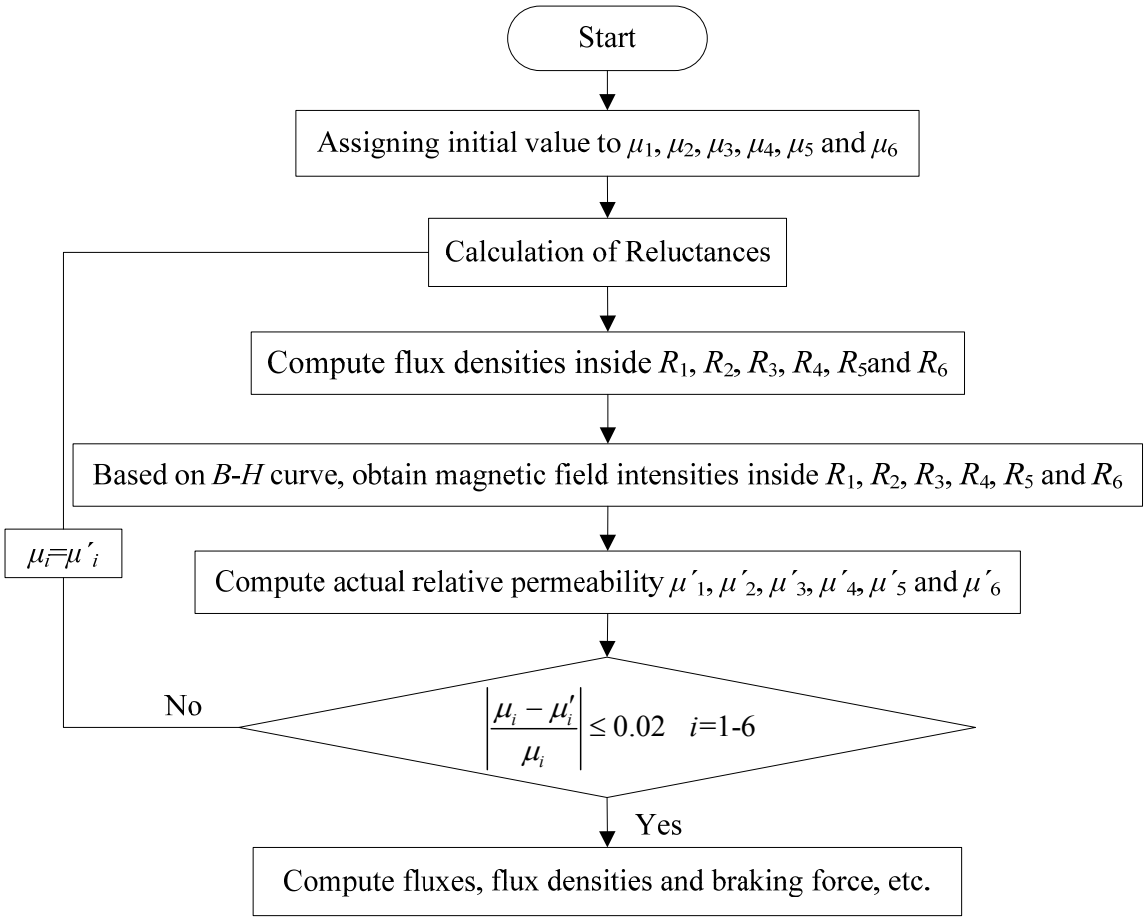

Figure 6. Iterative process of relative permeability.

Figure 7 compares the braking force obtained using the FEM with two different predicted curves for the braking force: the analytical method considering core saturation and the analytical method neglecting core saturation.

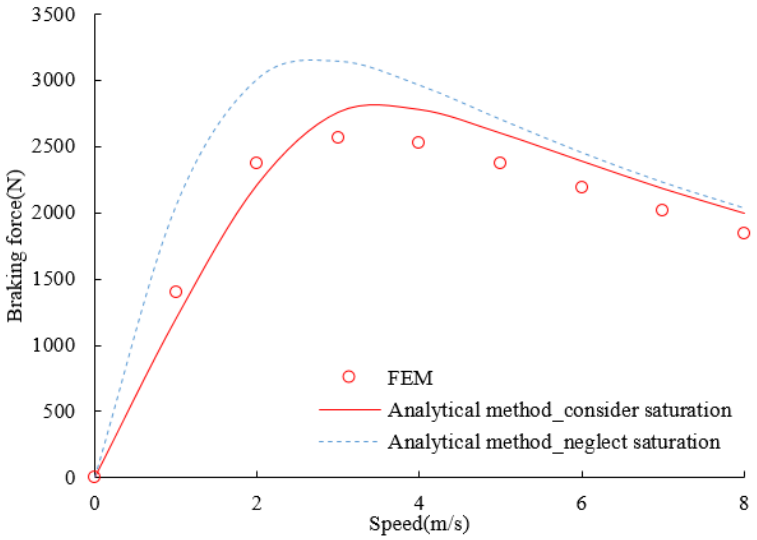

Figure 7. Braking force characteristic.

It can be seen that the difference between the analytical methods considering core saturation and neglecting core saturation is very obvious, especially in the low-speed region (in the high-speed region because of the eddy current reaction field, the saturation degree of the iron part is reduced). Therefore, in order to improve the accuracy of the analytical model, the saturation effects must be considered.

4. Parameter Analysis and Its Determination

In this section, the influence of several geometrical and physical parameters on the braking force is investigated to provide useful information to the designers of hybrid excitation eddy current brakes. The initial parameters of the hybrid excitation linear eddy current brake are shown in Table 1.

Table 1. Initial parameters of the hybrid excitation linear eddy current brake.

Symbol	Quantity	Value
h_m	width of the permanent magnet	18 mm
b_m	height of the permanent magnet	10 mm
I	excitation current	14 A
N	turns of the excitation winding	200
L	length of the primary iron core	200 mm
l_δ	width of the primary iron core	100 mm
h_j	height of the primary core yoke	11 mm
H	height of the primary iron core	49 mm
δ	air gap length	2 mm
τ	pole pitch	40 mm
c	conductor plate thickness	2 mm
h_b	back iron thickness	9 mm
b_t	tooth width	16 mm

4.1. Influence of the Air Gap Length

Figure 8 shows the braking force-speed characteristic with different air gap lengths. It can be seen that the braking force decreases gradually as the air gap increases, and this is because a large air gap length will result in a lower magnetic density. In addition, for a large air gap, the high-speed region is flatter than for a small air gap because the eddy currents are located farther from the primary part and thus have a lesser weakening influence on them. In order to obtain a larger braking force, the air gap length is chosen as 1 mm.

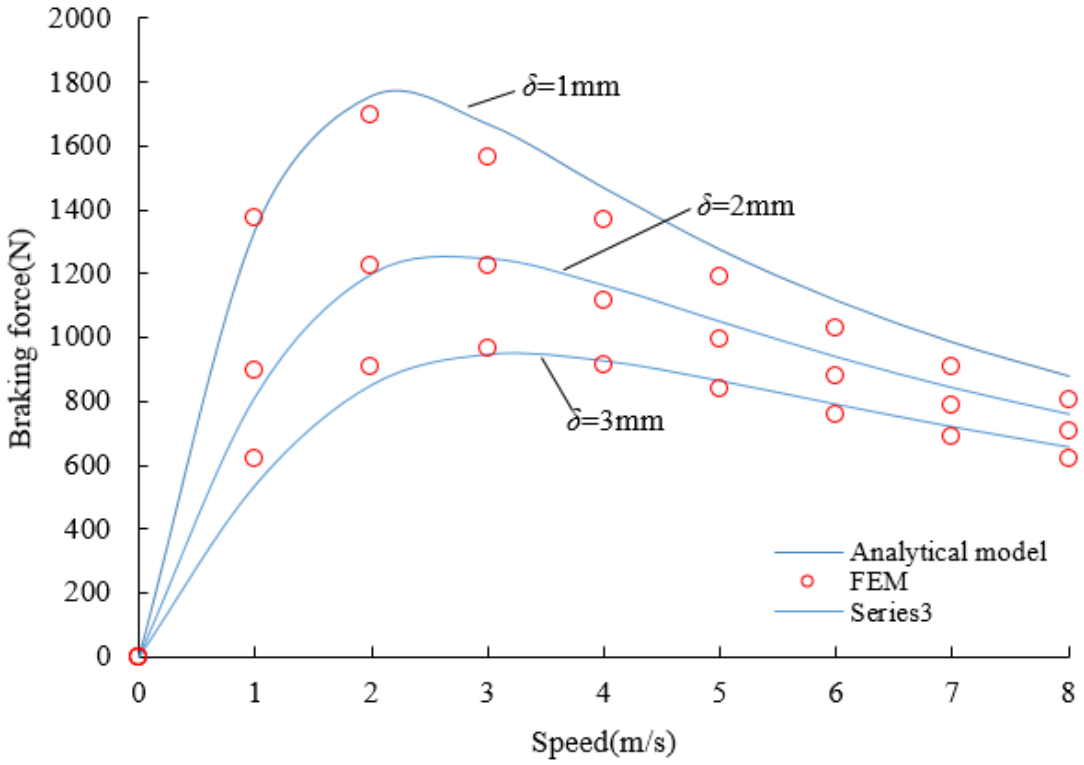

Figure 8. Braking force-speed characteristic for different air gap lengths.

4.2. Influence of the Conductor Plate Thickness

The secondary conductor plate is not only an important part of the magnetic circuit but also the medium of the eddy currents. As the conductor plate thickness increases, the machine air gap effectively increases (copper has a permeability of, essentially, the air); however, the increase of the conductor plate thickness results in the increase of the conductivity of the conductor plate. Figure 9 shows the braking force-speed characteristic with different conductor plate thicknesses. It can be seen that the increasing conductor plate thickness results in a lower peak braking force and smaller critical speed. In order to obtain a larger braking force, the conductor thickness is chosen as 1 mm.

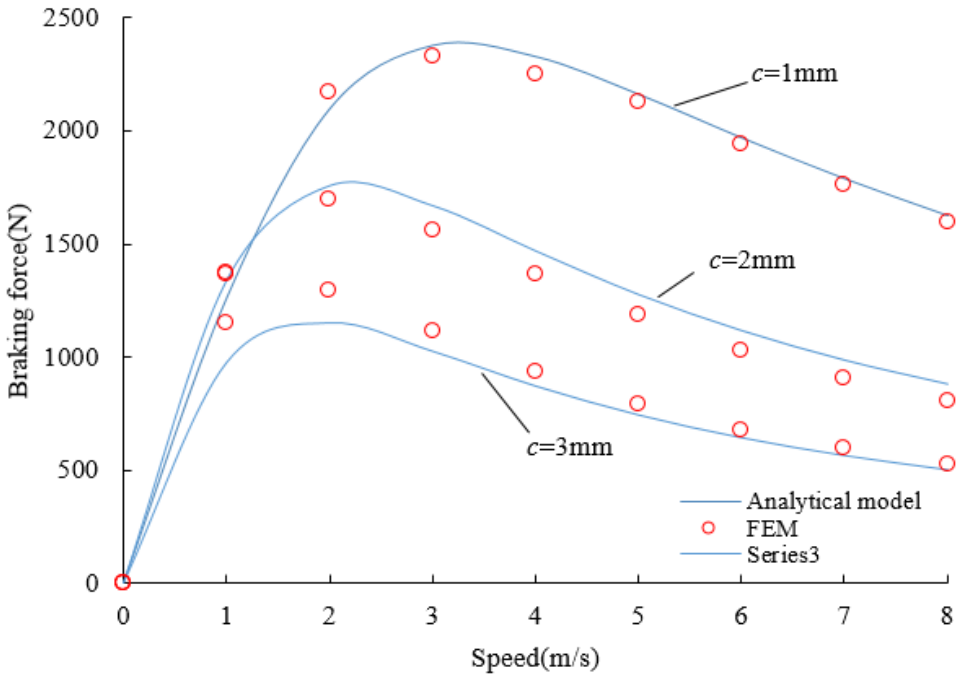

Figure 9. Braking force-speed characteristic for different conductor thicknesses.

4.3. Influence of the Conductor Material

Figure 10 shows the braking force-speed characteristic with different conductor materials. It can be seen that the slope of the braking force characteristic strongly depends on the conductivity of the conductor. The critical speed decreases as the conductivity of the conductor increases, and the conductivity has a small impact on the peak value of the braking force. Because of the limit of the experimental installation, the speed of the hybrid excitation linear eddy current brake can only take a smaller value. Therefore, the conductor material is chosen as copper.

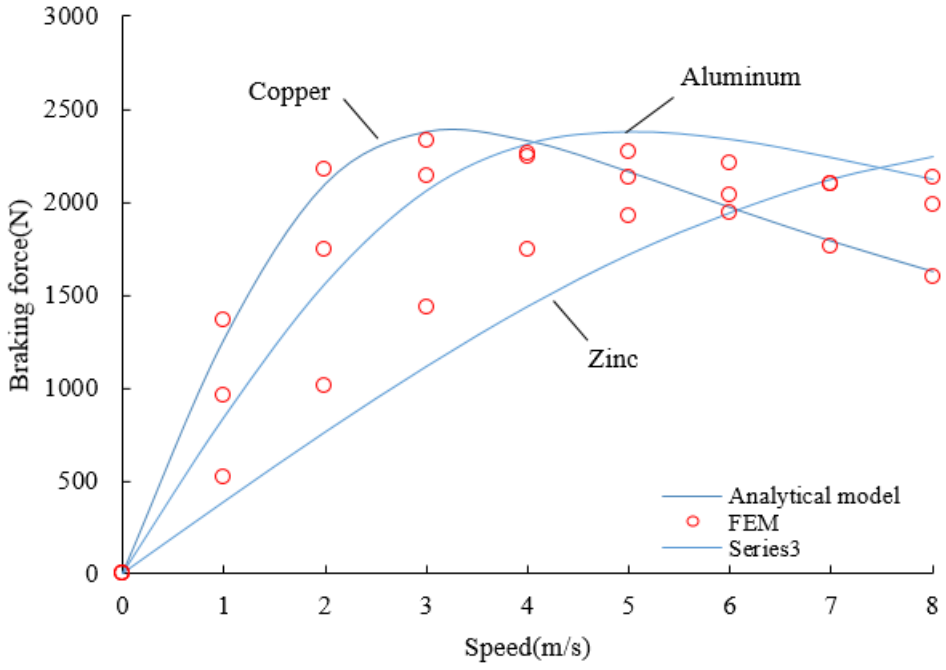

Figure 10. Braking force-speed characteristic for different conductor materials.

4.4. Influence of the Excitation Current

Figure 11 shows the braking force-speed characteristic with different excitation currents. It can be seen that the braking force increases gradually as the excitation current increases.

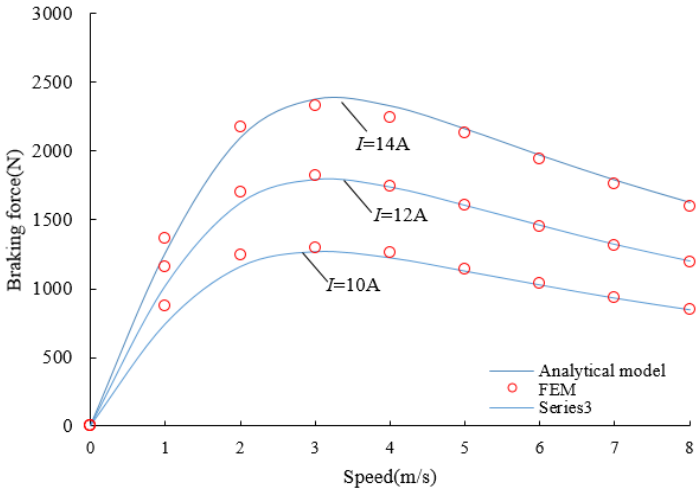

Figure 11. Braking force-speed characteristic for different excitation currents.

Moreover, the critical speed slightly increases as the excitation current increases. In order to obtain a larger braking force and guarantee the thermal stability of the hybrid excitation eddy current brake, the excitation current is chosen as 14 A.

4.5. Influence of the Magnet Dimension

The effect of the magnet dimensions (the width of the permanent magnets h_m and the height of the permanent magnets b_m) is analyzed as shown in Figure 12. The study has been performed considering a constant magnet volume. It can be seen that there are optimal magnet dimensions that will maximize the braking force density. The braking force density is the ratio of the braking force to the volume of the eddy current brake. In order to obtain a larger braking force density, the width of the permanent magnet is chosen as 13 mm and the height of the permanent magnet is chosen as 14 mm.

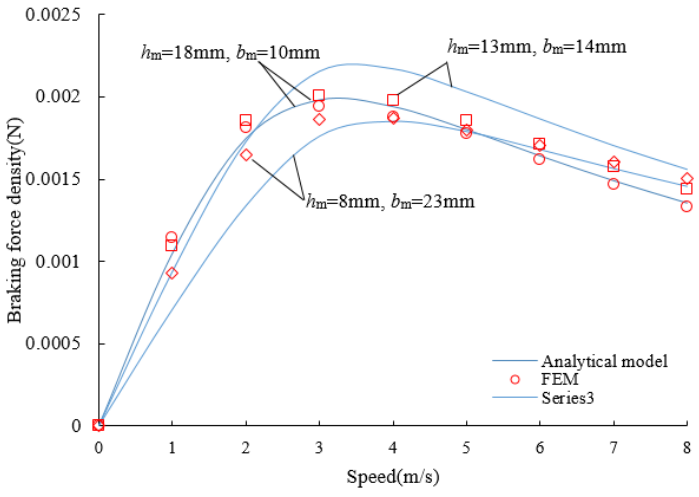

Figure 12. Braking force density-speed characteristic for different magnet dimensions.

5. Eddy Current Brake Controller

This paper presents a reliable and rugged controller of the hybrid excitation linear eddy current brake to control the amplitude of the braking force. Figure 13 shows the control scheme of the eddy current brake. There is an outer braking force controller and an inner current controller. The braking force controller outputs the reference excitation current I_{ref} according to the error between the reference braking force F_{ref} and the actual braking force F_{a}. The current controller outputs a reference voltage u_{ref} according to the error between the reference excitation current I_{ref} and the actual excitation current I_{a}. One can adjust the excitation current and move forward to adjust the braking force by controlling the reference voltage u_{ref}.

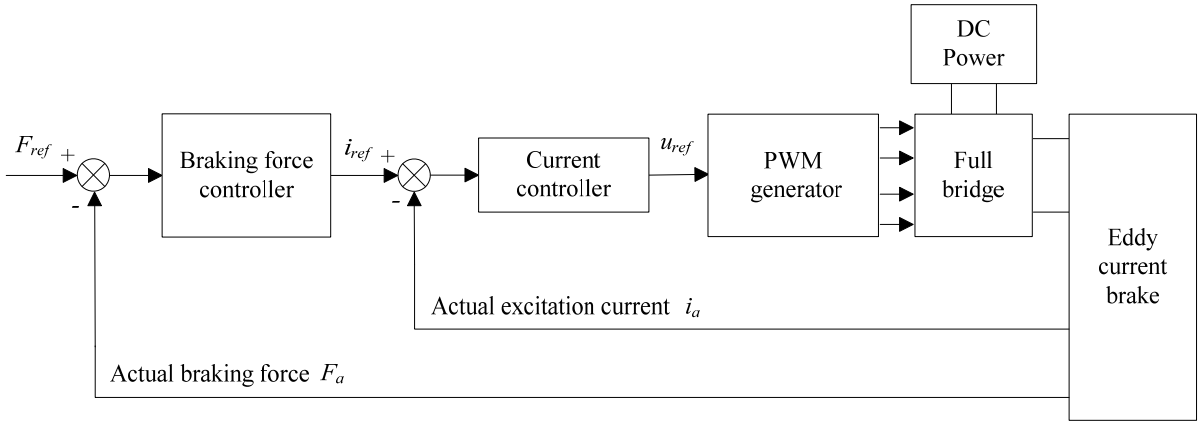

Figure 13. Control scheme of the eddy current brake.

5.1. Current Controller Design

In order to limit the amplitude of the current ripple to an acceptable extent, the three-level PWM scheme is used in this paper. For the three-level PWM scheme, the amplitude of the current ripple is independent of the direct current (DC)-link voltage, and the dynamic response characteristics of the eddy current brake system can be raised by increasing the DC-link voltage without increasing the current harmonics. Moreover, the switching frequency of an insulated gate bipolar transistor (IGBT) element is half of the output pulse frequency. This means that the switching frequency of the power elements is halved for a required dynamic performance of the eddy current brake compared with the two-level schemes.

5.2. Braking Force Controller Design

Dud to the saturation of the iron core, the relationship between the braking force and the excitation current is nonlinear. For the ease of control, the nonlinear curve is divided into several piecewise linear intervals. When the objective braking force F_{ref} is given, the corresponding interval is estimated firstly, then the corresponding excitation current I^* is calculated using the endpoints of the interval (I_1, F_1) and (I_2, F_2), as shown in Figure 14.

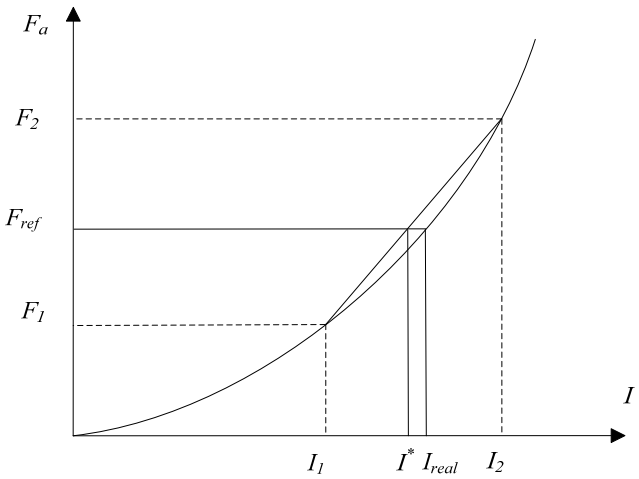

Figure 14. Schematic diagram of piecewise linearization.

The expression of I^* is shown below:

$$I^* = \frac{I_2 - I_1}{F_2 - F_1}(F_{\text{ref}} - F_1) + I_1 \tag{48}$$

Finally, the reference excitation current I_{ref} is shown as:

$$I_{ref} = I^* + \Delta I \tag{49}$$

where ΔI is the output of the proportion integration (PI) controller.

A block diagram of the braking force controller is shown in Figure 15. The input of the PI controller is the error signal between the objective braking force F_{ref} and the actual braking force F_{a}.

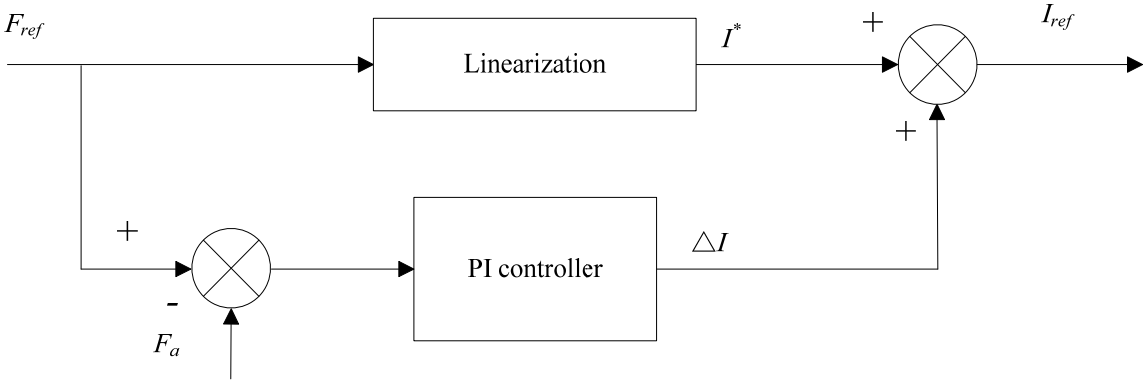

Figure 15. Block diagram of the braking force controller.

6. Numerical and Experimental Analysis

The 2-D finite element study is carried out in the same domain as the analytical problem. The field line distribution and the magnetic flux density map at a speed of 2 m/s are plotted in Figure 16a,b, respectively. It is observed that the reaction field of eddy currents tilts the field line entering the secondary conductor and shifts the epicenters of the flux density formation behind the centerlines of the magnets. Both the tilt and epicenter shift are a function of speed.

The braking force characteristics of the electric excitation eddy current brake and the hybrid excitation eddy current brake are compared at the same excitation current. The electric excitation eddy current brake has the same structure as the hybrid excitation eddy current brake, except that there are not permanent magnets, as shown in Figure 17.

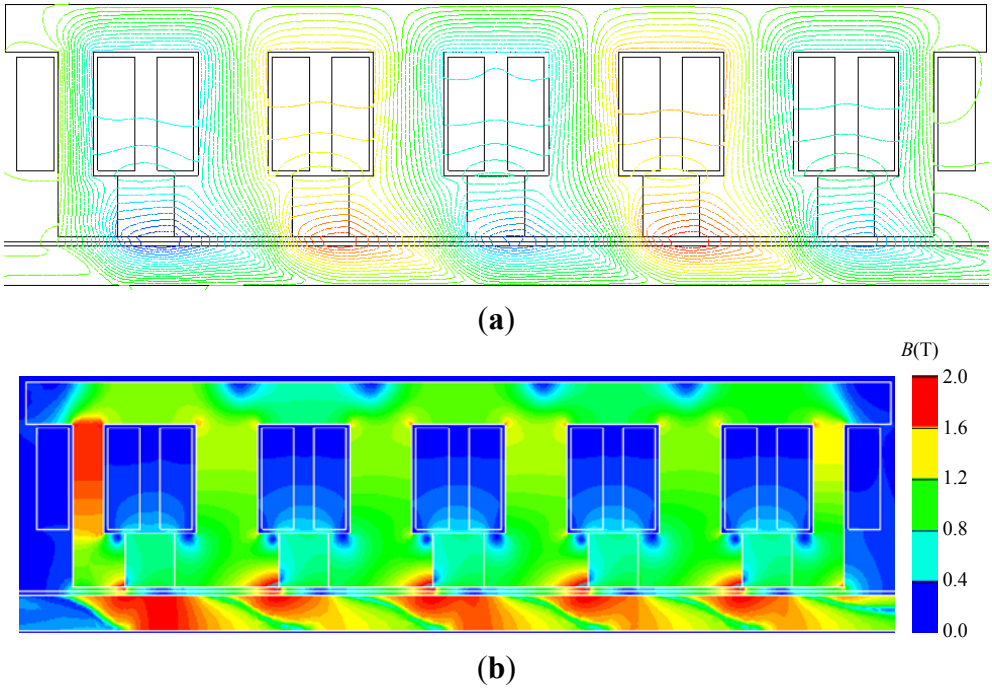

Figure 16. (**a**) Field line distribution and (**b**) the magnetic flux density map.

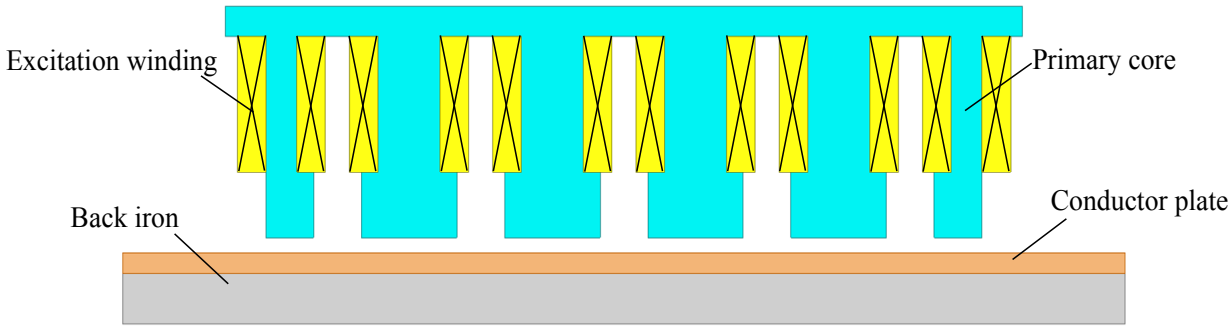

Figure 17. Structure of the electric excitation linear eddy current brake.

Figure 18a is the magnetic flux density map of the electric excitation eddy current brake at a speed of 2 m/s. The flux density of the gray area is larger than 2 T. Figure 18b is a comparison of the braking force characteristics of the electric excitation eddy current brake and the hybrid excitation eddy current brake.

As can be observed in Figure 18, the primary core of the electric excitation eddy current brake is saturated, but the primary core of the hybrid excitation eddy current brake is not saturated at the same excitation current, as shown in Figure 16b. Moreover, the braking force produced by the hybrid excitation eddy current brake is larger than that produced by the electric excitation eddy current brake. In other words, the excitation loss of the hybrid excitation eddy current brake is lower than that of the electric excitation eddy current brake under the same braking force level.

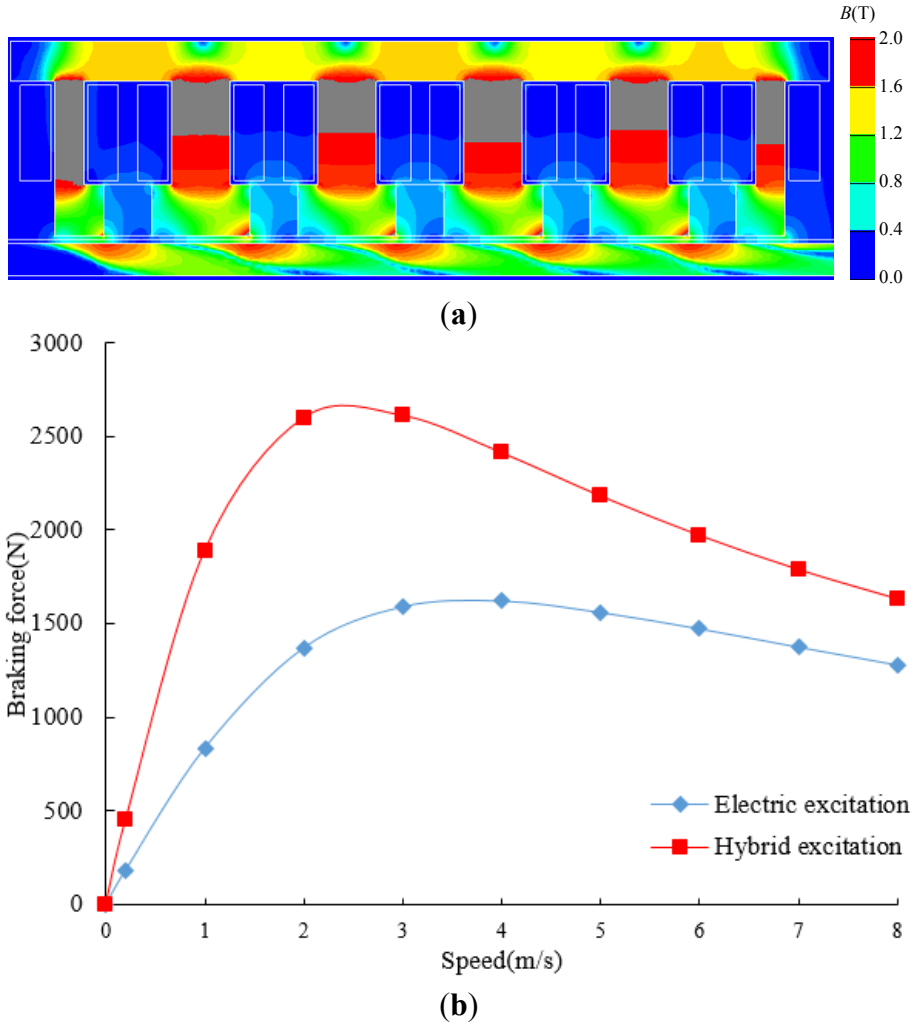

Figure 18. (**a**) Magnetic flux density map of the electric excitation eddy current brake and (**b**) a comparison between the electric excitation eddy current brake and hybrid excitation eddy current brake.

Therefore, we can conclude that the presence of the permanent magnets, whose flux lines in the primary core are oppositely directed with respect to the flux lines by the excitation windings, has the effect of mitigating the saturation of the iron in the teeth of the primary core. This allows the brake to be fed with more intense currents, improving the braking force. Through the above analysis, we can see that the hybrid excitation eddy current brake has many advantages, such as controllability, high force density and low excitation loss. The prototype of the hybrid excitation linear eddy current brake is shown in Figure 19a. The prototype includes the primary part and the secondary part. The primary part consisted of the iron core, excitation windings, permanent magnets, slides, cushion blocks, connecting plate and so on. The secondary part consisted of the conductor plate, back iron, slide rail and limited block. In this experiment, the rotation movement of a servo rotating motor is transformed into linear motion through a ball screw to drive the primary part of the eddy current brake. The test bed is shown in Figure 19b. It includes the servo rotating motor, a tension-compression sensor, the ball screw, the hybrid excitation linear eddy current brake and the controller. The measured value of the braking force can be obtained easily by measuring the output voltage of the tension-compression sensor. In this paper, the relationship between the output voltage of the tension-compression sensor and the braking force is as shown below.

$$F = \frac{V_{\text{out}}}{5\text{mV}} \tag{50}$$

In other words, when the output voltage of the tension-compression sensor is 5 mV, the braking force is 1 N.

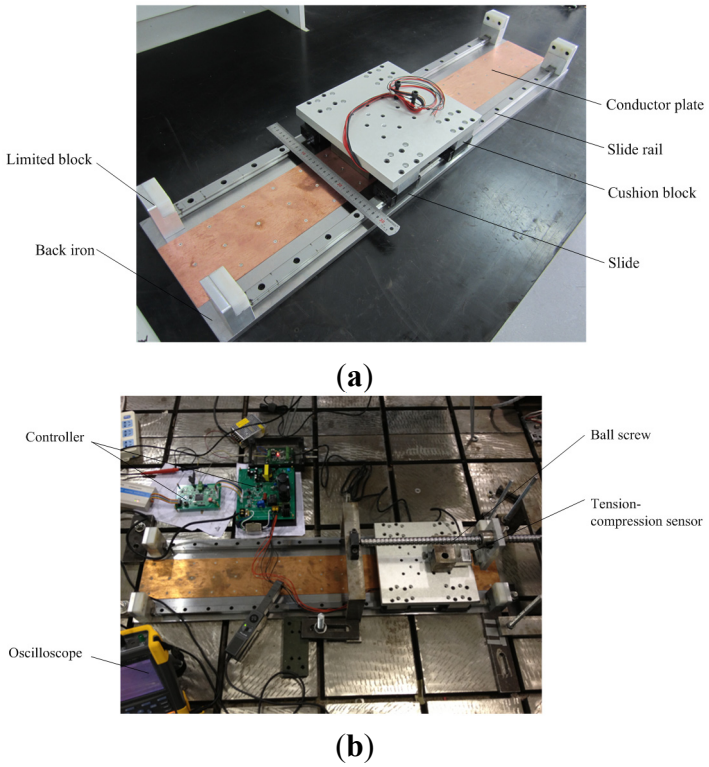

Figure 19. (**a**) Prototype of the hybrid excitation linear eddy current brake and (**b**) the test bed.

The final parameters of the hybrid excitation linear eddy current brake are shown in Table 2.

Table 2. Final parameter of the hybrid excitation linear eddy current brake.

Symbol	Quantity	Value
h_{m}	width of the permanent magnet	13 mm
b_{m}	height of the permanent magnet	14 mm
I	excitation current	14 A
N	turns of the excitation winding	200
L	length of the primary iron core	200 mm
l_{δ}	width of the primary iron core	100 mm
h_{j}	height of the primary core yoke	11 mm
H	height of the primary iron core	53 mm
δ	air gap length	1 mm
τ	pole pitch	40 mm
c	conductor plate thickness	1 mm
h_{b}	back iron thickness	9 mm
b_{t}	tooth width	16 mm

Figure 20 shows the experimental measurements of the braking force compared to the calculated values by finite element method. It can be seen that the agreement between the experimental measurements and the calculated values by the finite element method is very good. Moreover, due to the saturation of the iron core, the relationship between the braking force and the excitation current is nonlinear. As shown in Figure 19b, the length of the stator of the prototype is small, *i.e.*, the stroke of the prototype is limited. Therefore, the speed cannot reach a higher value. This problem will be solved in the future.

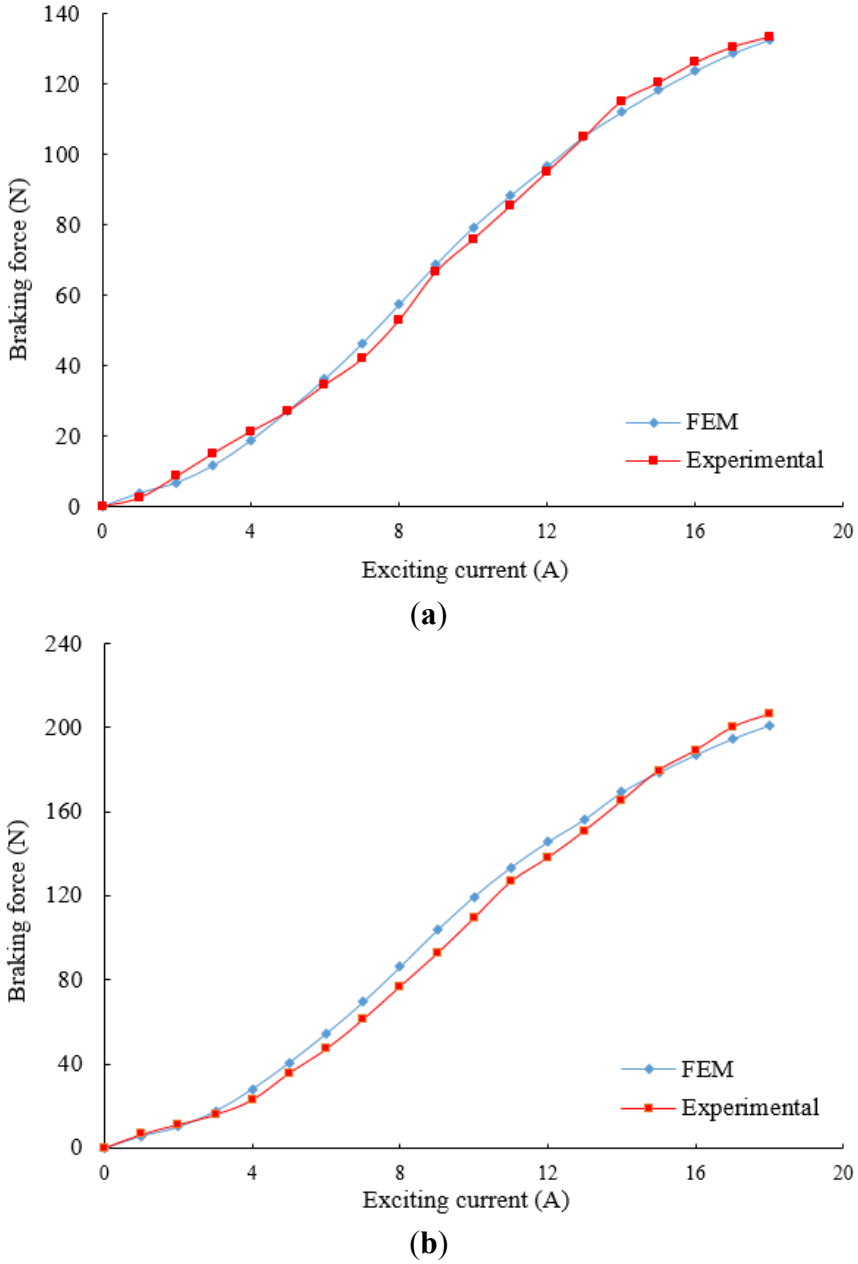

Figure 20. Comparison between the experimental measurements and calculated values via the finite element method: (**a**) $v = 0.1$ m/s and (**b**) $v = 0.15$ m/s.

The output current of the full bridge power converter with the two-level PWM schemes and the three-level PWM schemes are given in Figure 21a,b, respectively. The results show that the amplitude of the current ripple with the two-level PWM schemes is approximately 50 mA and

the amplitude of the current ripple with the three-level PWM schemes is approximately 12.5 mA. That is, the amplitude of the current ripple is significantly reduced by using the three-level PWM schemes. The experimental waveforms of the braking force are shown in Figure 21c–f. It can be seen that there is no overshoot in the braking force responses.

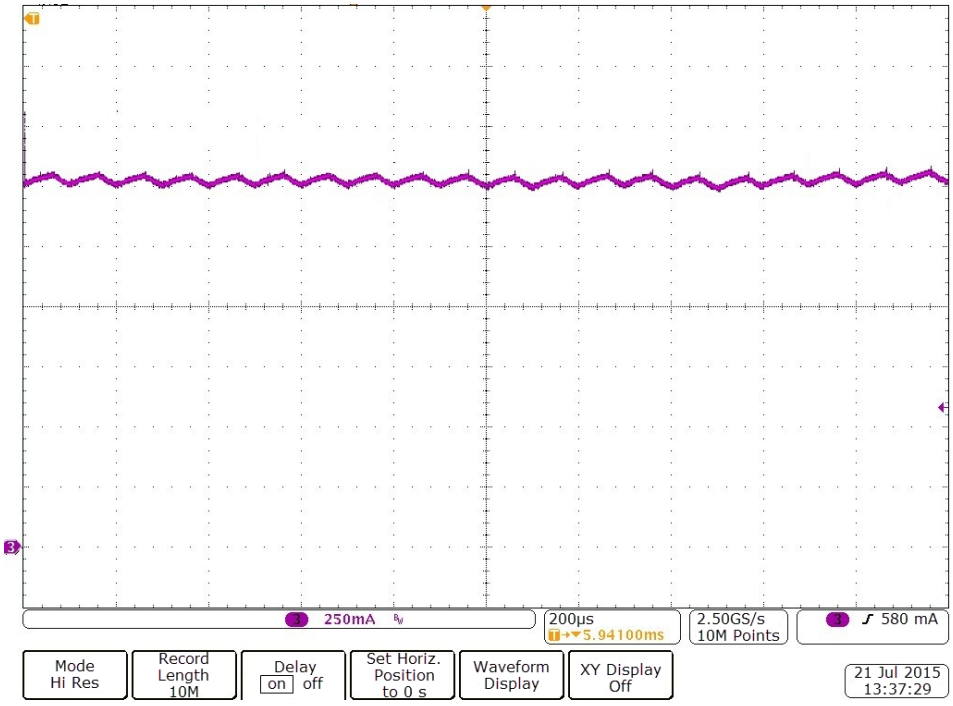

(**a**)

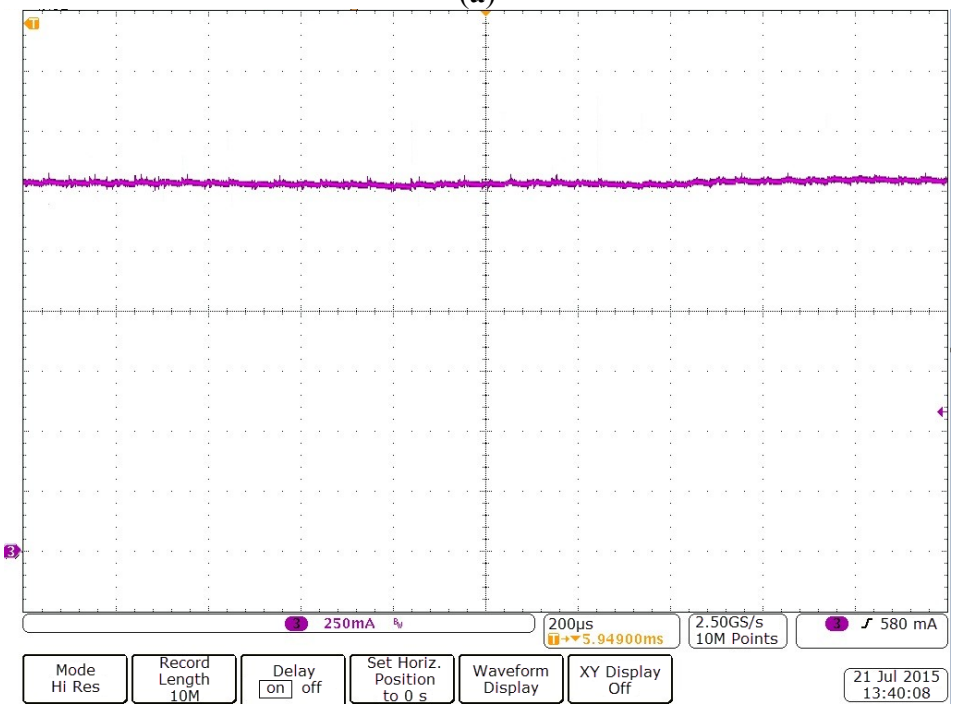

(**b**)

Figure 21. *Cont.*

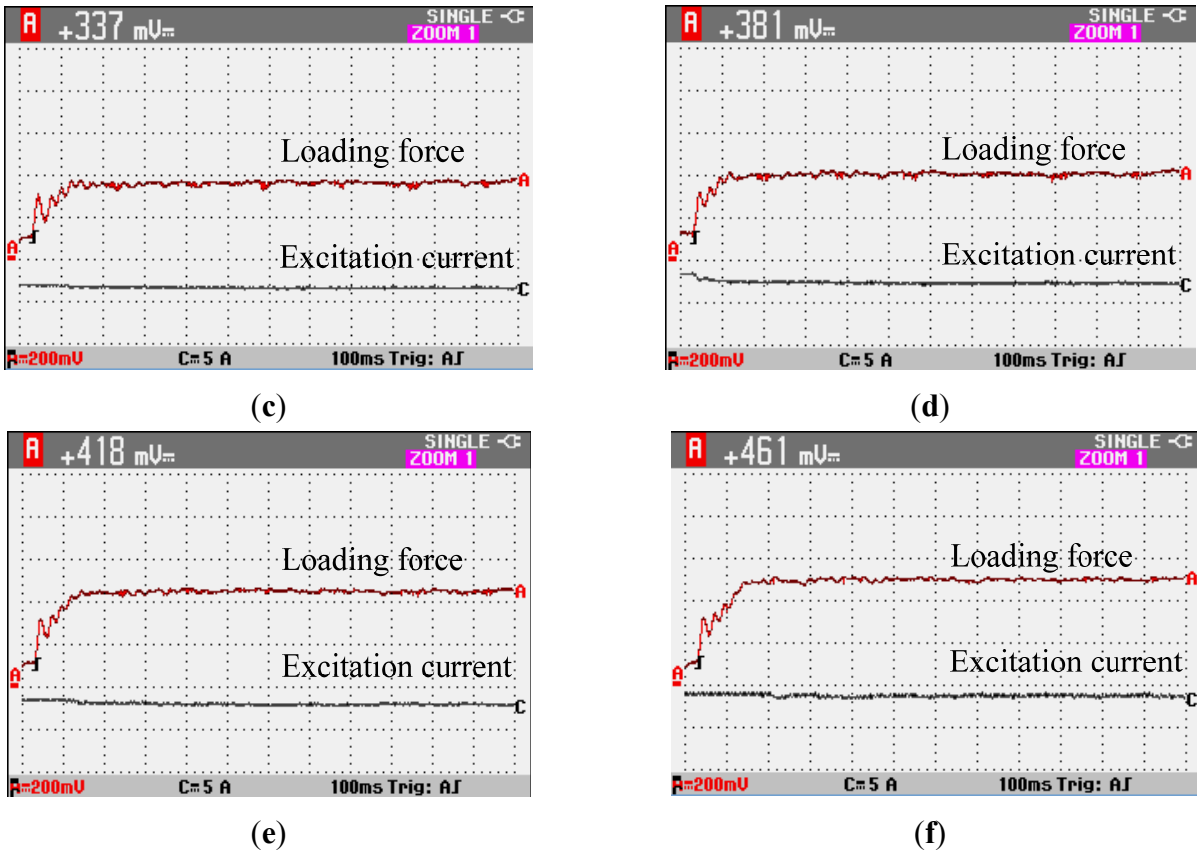

Figure 21. (**a**) Output current with the two-level PWM schemes; (**b**) output current with the three-level PWM scheme; (**c**) F_{ref} = 70 N; (**d**) F_{ref} = 80 N; (**e**) F_{ref} = 90 N and (**f**) F_{ref} = 100 N.

The objective braking force, the measured value of the output voltage of the tension-compression sensor, the measured value of the braking force and the error between the objective braking force and the measured value of the braking force are shown in Table 3.

Table 3. Analysis of the experimental results.

Objective Braking Force	Measured Value of Output Voltage	Measured Value of Braking Force	Error
70 N	337 mV	67.4 N	3.7%
80 N	381 mV	76.2 N	4.8%
90 N	418 mV	83.6 N	7.1%
100 N	461 mV	92.2 N	7.8%

As can be observed in Table 3, the measured value of the braking force has good correlation with the objective braking force, and the availability of the eddy current brake controller is verified.

7. Conclusions

In this paper, a novel hybrid excitation linear eddy current brake was presented. The hybrid excitation linear eddy current brake has the advantages of high force density and low excitation loss compared to the electric excitation linear eddy current brakes. The validity of the analytical model was verified by the FEM and experimental tests, therefore the analytical model can be used in the preliminary design of

eddy current brakes. Parametric analysis was performed to explore the influence of the design parameters on the eddy current brake performance. Moreover, the experimental results show that the eddy current brake can generate objective braking force using the controller proposed in this paper. It has been found that the proposed eddy current brake system can be used in road and rail vehicles.

Acknowledgments

This work was supported by National Science and Technology Major Projects (2012ZX04001-051).

Author Contributions

Baoquan Kou conceived the structural and experiments of the hybrid excitation eddy current brake. Lu Zhang, He Zhang and Yinxi Jin performed the experiments. Yinxi Jin analyzed the data and wrote the paper.

Conflicts of Interest

The authors declare no conflict of interest.

References

1. Jang, S.; Lee, S.; Jeong, S. Characteristic analysis of eddy-current brake system using the linear Halbach array. *IEEE Trans. Magn.* **2002**, *38*, 2994–2996.
2. Sainjargal, S.; Byun, J. Analysis and case study of permanent magnet arrays for eddy current brake systems with a new performance index. *J. Magn.* **2013**, *18*, 276–282.
3. Hecquet, M.; Brochet, P.; Lee, S.; Delsalle, P. A linear eddy current braking system defined by finite element method. *IEEE Trans. Magn.* **1999**, *35*, 1841–1844.
4. Gay, S.E. Contactless Magnetic Brake for Automotive Applications. Ph.D. Thesis, Texas A&M University, College Station, TX, USA, 2005.
5. Wang, P.J.; Chiueh, S.J. Analysis of eddy-current brakes for high speed railway. *IEEE Trans. Magn.* **1998**, *34*, 1237–1239.
6. Jang, S.; Lee, S. Comparison of three types of permanent magnet linear eddy-current brakes according to magnetization pattern. *IEEE Trans. Magn.* **2003**, *39*, 3004–3006.
7. Ha, K.; Hong, J.; Kim, G.; Lee, J.; Kang, D. A study of the design for touch free linear eddy current brake. *IEEE Trans. Magn.* **1999**, *35*, 4031–4033.
8. Ihm, H.; Lee, S.; Ham, S.; Lee, J. The influence of slit construction on the eddy current braking torque considered by 3D FEM analysis. In Proceedings of the International Conference on Electrical Machines and Systems, Wuhan, China, 17–20 October 2008; pp. 444–446.
9. Choi, J.; Shin, H.; Park, Y.; Jang, S. Torque analysis of axial flux PM type eddy current brake based on analytical field computations. In Proceedings of the International Conference on Electrical Machines and Systems, Beijing, China, 20–23 August 2011; pp. 1–5.
10. Amati, N.; Tonoli, A.; Canova, A.; Cavalli, F.; Padovani, M. Dynamic behavior of torsional eddy-current dampers: Sensitivity of the design parameters. *IEEE Trans. Magn.* **2007**, *43*, 3266–3277.

11. Lequesne, B.; Liu, B.; Nehl, T.W. Eddy-current machines with permanent magnets and solid rotors. *IEEE Trans. Ind. Appl.* **1997**, *33*, 1289–1294.
12. Shin, H.; Choi, J.; Cho, H.; Jang, S. Analytical torque calculations and experimental testing of permanent magnet axial eddy current brake. *IEEE Trans. Magn.* **2013**, *49*, 4152–4155.
13. Canova, A.; Vusini, B. Analytical modeling of rotating eddy-current couplers. *IEEE Trans. Magn.* **2005**, *41*, 24–35.
14. Mohammadi, S.; Mirsalim, M.; Vaez-Zadeh, S. Nonlinear modeling of eddy-current couplers. *IEEE Trans. Energy Convers.* **2014**, *29*, 224–231.
15. Li, P.; Ma, J.; Fang, Y. Design and analysis of hybrid excitation rail eddy current brake system of high-speed train. In Proceedings of the IEEE International Conference on Service Operations, Logistics, and Informatics, Beijing, China, 10–12 July 2011; pp. 565–569.
16. Edwards, J.D.; Jayawant, B.V.; Dawson, W.R.C.; Wright, D.T. Permanent-magnet linear eddy-current brake with a non-magnetic reaction plate. *IEE Proc. Electr. Power Appl.* **1999**, *146*, 627–631.
17. Jang, S.; Jeong, S.; Cha, S. The application of linear Halbach array to eddy current rail brake system. *IEEE Trans. Magn.* **2001**, *37*, 2627–2629.
18. Gay, S.E.; Ehsani, M. Analysis and experimental testing of a permanent magnet eddy-current brake. In Proceedings of IEEE Conference Vehicle Power and Propulsion, Chicago, IL, USA, 7–9 September 2005; pp. 756–765.
19. Canova, A.; Vusini, B. Design of axial eddy current couplers. *IEEE Trans. Ind. Appl.* **2003**, *39*, 725–733.
20. Yazdanpanah, R.; Mirsalim, M. Axial-flux wound-excitation eddy-current brakes: Analytical study and parametric modeling. *IEEE Trans. Magn.* **2014**, *50*, 1–10.
21. Choi, J.; Jang, S. Analytical magnetic torque calculations and experimental testing of radial flux permanent magnet-type eddy current brakes. *J. Appl. Phys.* **2012**, *111*, doi:10.1063/1.3672408.
22. Singh, A. Theory of eddy-current brakes with thick rotating discs. *Proc. IEE* **1977**, *124*, 373–376.
23. Park, M.; Choi, J.; Shin, H.; Jang, S. Torque analysis and measurements of a permanent magnet type Eddy current brake with a Halbach magnet array based on analytical magnetic field calculations. *J. Appl. Phys.* **2014**, *115*, doi:10.1063/1.4862523.
24. Srivastava, R.K.; Kumar, S. An alternative approach for calculation of braking force of an eddy-current brake. *IEEE Trans. Magn.* **2009**, *45*, 150–154.
25. Liu, Z.J.; Vourdas, A.; Binns, K.J. Magnetic field and eddy current losses in linear and rotating permanent magnet machines with a large number of poles. *IEE Proc.* **1991**, *138*, 289–294.